Independent and coherent transitions between antiferromagnetic states of few-molecule systems

Claire Besson [1,2,3] Philipp Stegmann [4,5] Michael Schnee,[2,3] Zeila Zanolli [6,7] Simona Achilli,[7,8] Nils Wittemeier [7]
Asmus Vierck,[9] Robert Frielinghaus,[2,3] Paul Kögerler [2,3,10] Janina Maultzsch [9,11] Pablo Ordejón,[7] Claus M. Schneider,[2,3]
Alfred Hucht [5] Jürgen König [5] and Carola Meyer [12,2,3,*]

[1]*Department of Chemistry, The George Washington University, Washington, DC 20052, USA*
[2]*Peter Grünberg Institut (PGI-6), Forschungszentrum Jülich, 52425 Jülich, Germany*
[3]*Jülich Aachen Research Alliance (JARA)—Fundamentals of Future Information Technology, 52425 Jülich, Germany*
[4]*Department of Chemistry, Massachusetts Institute of Technology, Cambridge, Massachusetts 02139, USA*
[5]*Theoretische Physik, Universität Duisburg-Essen and CENIDE, 47048 Duisburg, Germany*
[6]*Condensed Matter and Interfaces, Debye Institute for Nanomaterials Science and European Theoretical Spectroscopy Facility (ETSF),
Utrecht University, Princetonplein 1, 3584 CC Utrecht, The Netherlands*
[7]*Catalan Institute of Nanoscience and Nanotechnology—ICN2 (CSIC-BIST) Campus UAB, Bellaterra, 08193 Barcelona, Spain*
[8]*Dipartimento di Fisica "Aldo Pontremoli" and European Theoretical Spectroscopy Facility (ETSF), Universitá degli Studi di Milano,
Via Celoria 16, Milan, Italy*
[9]*Institut für Festkörperphysik, Technische Universität Berlin, Hardenbergstrasse 36, 10623 Berlin, Germany*
[10]*Institute of Inorganic Chemistry, RWTH Aachen University, 52074 Aachen, Germany*
[11]*Department of Physics, Friedrich-Alexander-Universität Erlangen-Nürnberg (FAU), Staudtstrasse 7, 91058 Erlangen, Germany*
[12]*School of Mathematics/Computer Sciences/Physics, Institute of Physics, Universität Osnabrück, 49069 Osnabrück, Germany*

Spin-electronic devices are poised to become part of mainstream microelectronic technology. Downsizing them led to the field of molecular spintronics. Here, we provide proof-of-concept data that allow expanding this area from its traditional focus on single-molecule magnets to molecules in which spin centers are antiferromagnetically (AFM) coupled to result in a singlet ground state. In this context, and in contrast to all previous work on molecular spintronics, we develop a detection scheme of the spin state of the molecule that does not rely on a magnetic moment. Instead, we use quantum dot devices consisting of an isolated, contacted single-wall carbon nanotube covalently bound to a limited number of molecular AFMs, for which we chose representative coordination complexes incorporating four Mn(II) or Co(II) ions. Time-dependent quantum transport measurements along the functionalized nanotube show steplike transitions between several distinct current levels that we attribute to transitions between different AFM states of individual molecular complexes grafted on the nanotube. A statistical analysis of the switching events using factorial cumulants indicates that the cobalt complexes switch independently from each other, whereas a coherent superposition of the AFM spin states of the molecules along the nanotube is observed for the manganese complexes. The long coherence time of the superposition state (several seconds at 100 mK) is made possible by the absence of spin and orbital momentum in the relevant states of the manganese complex, while the cobalt complex includes a significant orbital momentum contribution due to the pseudo-octahedral coordination environment of the d^7 metal centers.

I. INTRODUCTION

Antiferromagnetic (AFM) spintronics is emerging as a promising field for technologies ranging from magnetic random access memories to neuromorphic computing and terahertz information devices, as AFMs do not produce and are insensitive toward magnetic stray fields [1–4]. The lack of a net magnetic moment confers high stability to the AFM states but, at the same time, makes it challenging to address and differentiate among them. Therefore, this area has not yet been extended to the level of individual molecules exhibiting AFM coupled magnetic spin centers, while spintronics with, e.g., high-spin single-molecule magnets (SMMs) are well established [5,6]. In this paper, we showcase how transitions between distinct molecular states with $S_{tot} = 0$ can be monitored via charge transport when the molecules are coupled to a carbon nanotube (CNT) quantum dot in field effect geometry. Transitions between different AFM states are accompanied by steplike changes of the current through the quantum dot, resulting in a random telegraph signal (RTS). We analyze the signal statistics employing factorial cumulants, which are well established in the field of quantum optics but have not yet been widely applied in transport. This method of investigation paves the way to exploring the molecular
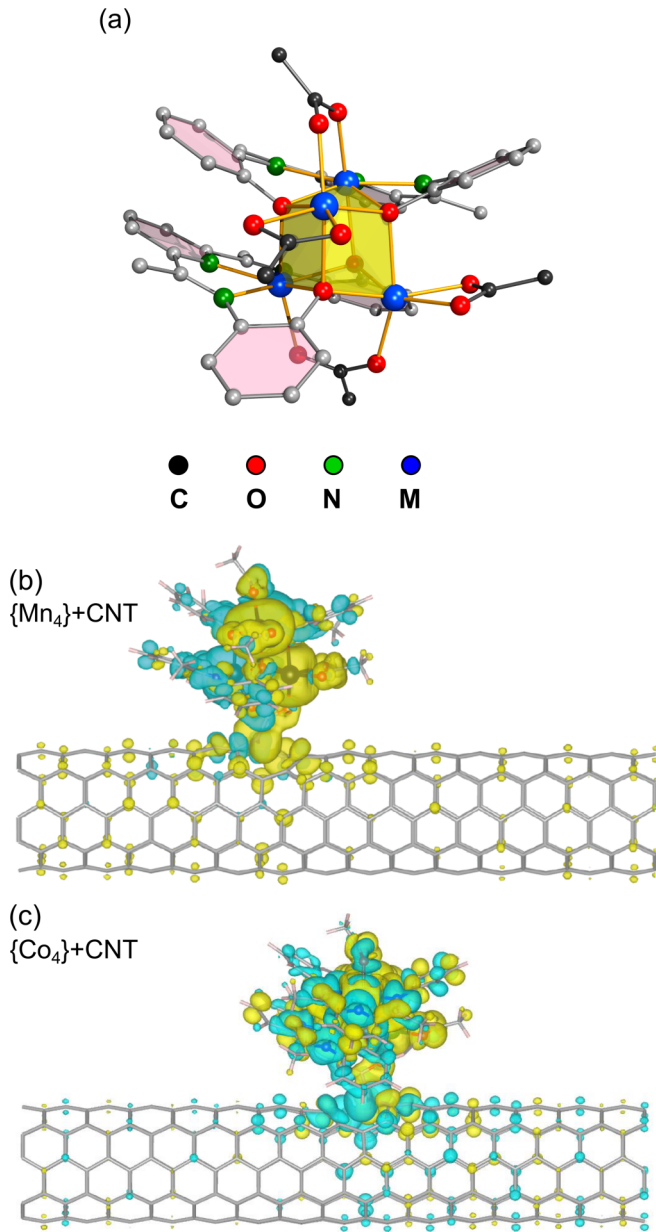
*carola.meyer@uni-osnabrueck.de

(a)

- ● **C**
- ● **O**
- ● **N**
- ● **M**

(b)
{Mn$_4$}+CNT

(c)
{Co$_4$}+CNT

FIG. 1. (a) General structure of the metal complexes (M: metal ion). H is omitted for clarity, the central (distorted) M$_4$O$_4$ cubane highlighted in yellow, all coordinative bonds in orange. All aromatic rings are made transparent to improve spatial representation. Ligand backbones differentiate between chelate and acetate ligands. Spin density ($\rho_\uparrow - \rho_\downarrow$) on (b) the carbon nanotube {Mn$_4$}-(CNT) and (c) the {Co$_4$}-CNT hybrid system computed from first principles in an open-system setup [7–9]. Light blue and yellow indicate positive and negative values of the isosurfaces normalized to the maximum spin density.

equivalent of AFM spintronics by employing states that do not couple to fluctuations of external magnetic fields, thereby allowing for long-lived superposition states. In this paper, we study two structurally identical molecular systems that differ fundamentally only in the spin-carrying metal ions (Fig. 1). Modeling the RTS, we find that, in the absence of spin-orbit

coupling, such states can exhibit a coherent superposition with exceptionally long coherence time.

In the past years, significant progress has allowed detection of spin states of individual molecules using scanning tunneling microscopy [10–20] or molecules in junctions [21–24]. However, in these approaches, the electric bias field applied to the molecule will in general influence its charge state and therefore its magnetic characteristics. To circumvent this issue, it has been proposed to detect the spin state of an SMM by grafting it to a nonmagnetic one-dimensional conductor (such as a CNT) and measuring the magnetic state of the so-obtained hybrid system [25]. CNTs have been used successfully to read out states of SMMs by measuring the magnetoresistance effect [26] and detecting phonon-spin interaction [27] and spin interactions within an individual SMM [28]. All these experiments depend on the detection of a local magnetic moment. Therefore, they cannot be employed for single-molecule AFMs that have no resulting magnetic moment. Here, we show that devices functionalized with AFM molecules that differ only in the spin-carrying metal ions exhibit RTSs with distinct statistics that reveal whether the transitions between different current levels are correlated. We interpret the RTS in terms of transitions between different molecular $S_{\text{tot}} = 0$ eigenstates.

II. RESULTS AND DISCUSSION

A. Electronic and magnetic structure of the CNT-AFM hybrid

To fabricate a system that exhibits distinct molecular $S_{\text{tot}} = 0$ states, we use charge-neutral molecular [M$_4$L$_2$(OAc)$_4$] complexes [29,30] (H$_2$L = 2,6-bis-[1-(2-hydroxyphenyl)iminoethyl]-pyridine; HOAc = acetic acid; M = Mn$^{\text{II}}$ or Co$^{\text{II}}$). Those complexes (hereafter denoted as {Mn$_4$} and {Co$_4$}) are nearly isostructural and display a quasitetrahedral core of divalent metal ions interlinked by ligands [Fig. 1(a)]. Exchange coupling between the metal ions is mediated mainly by four oxygen atoms of the ligands, each bridging between three metal centers into a nearly cubic M$_4$O$_4$ core, which can be thought of as two pairs of AFM interacting ions. Two of the four ions reside in an approximately octahedral ligand field and two in an approximately trigonal bipyramidal ligand field with a spin $S = \frac{5}{2}(S = \frac{3}{2})$ for Mn$^{\text{II}}$ (Co$^{\text{II}}$). The ground state is AFM, as supported by magnetization measurements for the pristine molecules as well as for molecules grafted to CNTs [29–31]. Density functional theory (DFT) calculations of the isolated complexes [30] also yield an $S_{\text{tot}}^z = 0$ ground state, confirming the overall AFM nature of the intramolecular magnetic interactions in the simpler one-electron approximation. The complexes retain their AFM nature when grafted covalently to the CNT [Figs. 1(b) and 1(c)] by a metathesis reaction between an acetate ligand of the complex and a carboxylic acid group generated by oxidation of the tube [31]. Our DFT calculations confirm the overall AFM nature of the ground state of the grafted complexes and demonstrate that the interaction between each individual molecule and the CNT is similar for {Co$_4$} and {Mn$_4$}: The electronic properties of the nanotube around the Fermi energy are slightly perturbed by the molecule, and the total spin polarization of the hybrid system is larger for {Co$_4$}-CNT

than for {Mn$_4$}-CNT (Sec. SI-2 in the Supplemental Material [32] and Refs. [33–38] therein). We used an open-system approach [7–9] to demonstrate that the spin polarization induced by magnetic exchange interaction between the spins of the molecule and the spin of the electron in the CNT quantum dot at the grafting site is long-ranged ([Figs. 1(b) and 1(c)] and Sec. SI-2 in the Supplemental Material [32]).

Note that spin configurations with different total spin ($S_\text{tot} > 0$) lie several millielectronvolts above the ground state for both complexes (Tables S1 and S2 and Sec. SI-2 in the Supplemental Material [32]). This is at least two orders of magnitude larger than the energy involved in the low-temperature transport experiments presented here. Instead, we have to think of the AFM ground states with $S_\text{tot} = S_\text{tot}^z = 0$ in terms of a total spin of the complex $\vec{S}_\text{tot} := \sum_i \vec{S}_i$ characterized by the spin quantum number S_tot and the magnetic quantum number S_tot^z. To form a complete set of quantum numbers, we (arbitrarily) group the four individual ion spins into two pairs and include the spin quantum numbers S_{12}, S_{34} of the two spin pairs $\vec{S}_{ij} := \vec{S}_i + \vec{S}_j$ so that $\vec{S}_\text{tot} := \vec{S}_{12} + \vec{S}_{34}$ (Fig. S1 and Sec. SI-1 in the Supplemental Material [32]). We assume a pair-wise Heisenberg spin-exchange coupling, $H = -\frac{1}{2} \sum_{i \neq j} J_{ij} \vec{S}_i \cdot \vec{S}_j$ with AFM $J_{ij} < 0$. If all exchange couplings are equal, $J_{ij} = J$, the eigenenergy $E = -\frac{J}{2}[S_\text{tot}(S_\text{tot} + 1) - 4S(S + 1)]$ only depends on the spin quantum number S_tot of the total spin but not on S_tot^z, S_{12}, or S_{34}. For AFM couplings, $J < 0$, the ground state has total spin $S_\text{tot} = 0$ with vanishing dipole moment $S_\text{tot}^z = 0$, exhibiting a sixfold (fourfold) degeneracy for {Mn$_4$} ({Co$_4$}). The four degenerate states for {Co$_4$} would correspond to $|S_\text{tot}, S_\text{tot}^z, S_{12}, S_{34}\rangle = |0, 0, 0, 0\rangle, |0, 0, 1, 1\rangle, |0, 0, 2, 2\rangle, |0, 0, 3, 3\rangle$, to which the $|0, 0, 4, 4\rangle$ and $|0, 0, 5, 5\rangle$ states would be added for {Mn$_4$} (Sec. SI-1 in the Supplemental Material [32]). However, the degeneracy is lost in the actual molecules because the exchange interactions J_{ij} are not equivalent. This enables low-energy transitions within the now split $S_\text{tot} = S_\text{tot}^z = 0$ manifold (an example for an excited state is given in Sec. SI-1 in the Supplemental Material [32]) that cause a RTS in the current through the CNT quantum dot.

A key difference between the two molecules is the value of the orbital angular momentum $\langle L \rangle$, which is finite in Co$^\text{II}$, in agreement with the $3d^7$ atomic configuration and the respective ligand fields, but almost negligible in Mn$^\text{II}$ due to the half-filling of the $3d$ shell. By including spin-orbit coupling in the DFT calculations, we verified that the orbital angular momentum of cobalt is practically fully quenched for the two trigonal bipyramidal metal centers, while a significant orbital moment (0.18 and 0.25 μ_B, open-system approach) is found for the two octahedrally coordinated atoms (Sec. SI-2 in the Supplemental Material [32]).

B. Device preparation and characterization

Individual CNTs functionalized with either {Mn$_4$} or {Co$_4$} complexes are contacted in a field-effect-transistor structure with highly doped silicon serving as a back gate. Basic device characterization and fabrication details for the {Mn$_4$}-based device have been published elsewhere [39]. A similar procedure was used for {Co$_4$}-based device fabrication. The number of complexes within a device is derived from our
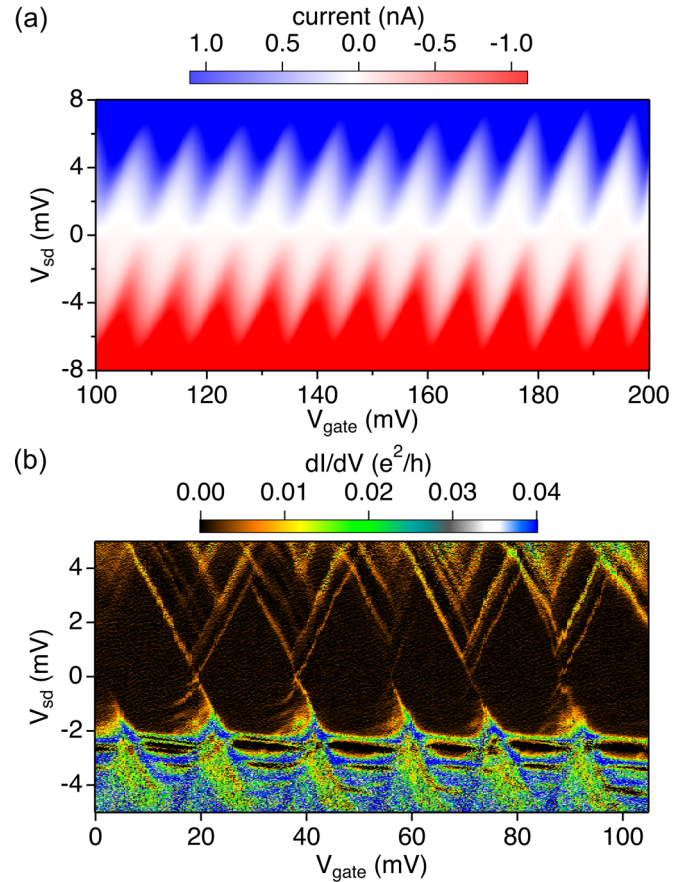

FIG. 2. (a) Stability diagram of the quantum dot formed on the {Mn$_4$}-functionalized carbon nanotube (CNT), measured at a temperature of 4 K ($B = 0$ T), exhibiting a very clean and regular pattern of Coulomb diamonds with a quantum dot size comparable with the distance between the electrodes [39]. (b) Coulomb diamonds of a CNT quantum dot functionalized with {Co$_4$} complexes at 100 mK ($B = 0$ T). The width of the current steps as well as that of the Coulomb peaks yield an electron temperature of 600 mK ($\sim$50 μeV).

previous experimental evaluation [31] of the functionalization density—approximately one complex every 10 nm, meaning negligible through-space interaction between neighboring complexes. Analysis of Raman spectroscopy based on the G-mode [40] and on the TO+ZA combination mode [41] of the device with {Mn$_4$} complexes suggests a zigzag (15,0) metallic CNT (Fig. S4 and Sec. SI-3 in the Supplemental Material [32]). Accordingly, no transport gap is found in the electrical measurements. This is consistent with our first-principles prediction of a metallic character for the hybrid CNT-{M$_4$} systems (Fig. S2 and Sec. SI-2 in the Supplemental Material [32]). The stability diagrams of the quantum dots bearing $\sim$50 {Mn$_4$} complexes or $\sim$70 {Co$_4$} complexes exhibit regular Coulomb diamonds (Fig. 2). Figure 2(a) shows the stability diagram of the {Mn$_4$}-functionalized quantum dot measured at $T = 4$ K. Since excited states are not resolved, we use a charging energy of $E_\text{ch} \sim 4$ eV to get a rough estimate of the length of the CNT quantum dot with $l \sim 350$ nm [39,42]. The stability diagram of the quantum dot functionalized with {Co$_4$} complexes was measured at base temperature of the dilution refrigerator [$T \approx 100$ mK, Fig. 2(b)]. Here, excited
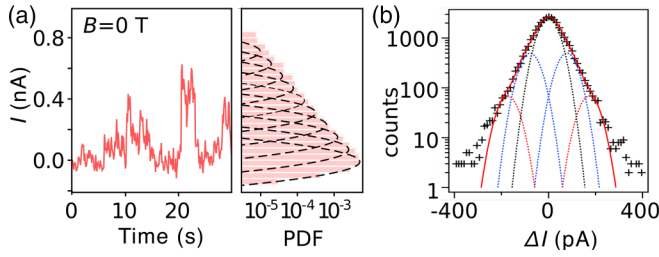
FIG. 3. (a) Short section of the time trace of the current at the edge of a Coulomb diamond of the {Mn$_4$}-functionalized carbon nanotube (CNT) quantum dot and probability density function (PDF) of the entire 3600 s signal displayed with 11 Gaussian peaks indicating the current levels (we omit the three highest levels for better visibility). (b) Histogram of the derivative of the entire signal (note the logarithmic scale) fitted with five Gaussian peaks leading to a standard deviation of the direct signal $\sigma_{direct} = \sigma_{deriv}/\sqrt{2} = 40(1)\,pA$, respectively.

states are nicely resolved, and thus, a more accurate estimate of the quantum dot length is derived from the first excited state at $\Delta E = 0.7\,meV$ yielding $l = 714\,nm$. The length estimates from the stability diagram fit reasonably well with the designed distance between the electrodes of 500 nm for the {Mn$_4$} device and of 700 nm for the {Co$_4$} device. We thus conclude that the covalent grafting of complexes to the CNT does not cause strong localization within the devices.

C. Analysis of the RTSs

Figure 3(a) shows on the left a short section of the current trace taken at the base temperature of the dilution refrigerator at the edge of the Coulomb diamond of a {Mn$_4$}-functionalized CNT device, displaying a characteristic RTS. The probability density function (PDF) corresponding to the entire trace (3600 s length), reported in Fig. 3(a), exhibits a quasiexponential decay instead of a single Gaussian peak expected for simple noise. A similar signal is measured at an equivalent position of a CNT quantum dot functionalized with {Co$_4$} complexes (Fig. 4). While it clearly does not resemble a single Gaussian peak, the asymmetry of the PDF is much less prominent than the {Mn$_4$} device, and the signal decays much faster, indicating the presence of a smaller number of levels for the signal.
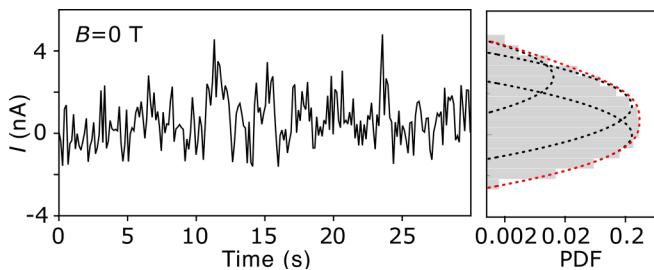

FIG. 4. Short section of the current trace at the edge of a Coulomb diamond of the {Co$_4$}-functionalized carbon nanotube (CNT) quantum dot and corresponding probability density function (PDF) of the entire signal (1300 s) with three Gaussian peaks fitted at $B = 0\,T$.
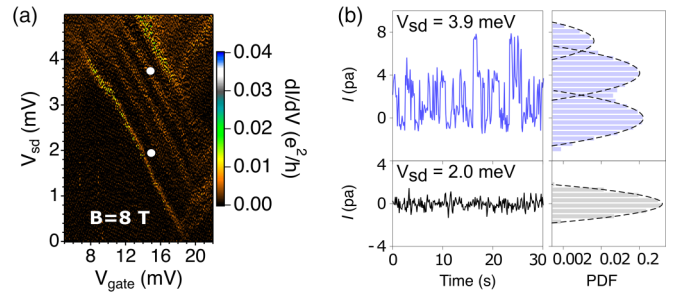

FIG. 5. (a) Part of the stability diagram of a carbon nanotube (CNT) quantum dot functionalized with ~70 {Co$_4$} complexes at $B = 8\,T$ (perpendicular to CNT axis). White dots indicate the positions where the current traces shown in (b) were measured (gate and bias voltage of the lower point the same as in Fig. 4). (b) Parts of the time traces of the current taken at the indicated positions in a (top, in blue, for $V_{sd} = 3.9\,mV$, bottom, in black, for $V_{sd} = 2.0\,mV$) with the respective probability density function (PDF) of the entire direct current traces after background correction on the right. Discrete current levels are indicated by dashed lines.

Studying the derivative of the direct current signal of the {Mn$_4$} device [see Fig. 3(b)] with respect to time, we extract the largest possible value between two current levels to be $\Delta I \sim 80\,pA$ and the standard deviation of $\sigma_{deriv} = \sqrt{2}\,\sigma_{direct} = 56.4(1.3)\,pA$, with the standard deviation of the direct signal σ_{direct} (see Sec. SI-4 in the Supplemental Material [32] for an extended discussion). The PDF of the direct current signal can thus be fitted by equidistant Gaussian peaks with full width at half maximum $= 2\sqrt{2\ln(2)}\sigma_{direct} = 94\,pA$. This results in at least 14 equidistant current levels. Each level is directly related to an energy that can be evaluated from the current-voltage curve taken at this gate voltage. We find a maximum spacing of $\Delta\varepsilon \sim 27\,\mu eV$. (The level spacing $\Delta\varepsilon$ might in fact be smaller, but this is beyond our resolution. This would lead to more levels but in fact leave the main results discussed below qualitatively unchanged.)

The PDF of the RTS signal in the {Co$_4$}-functionalized devices (Fig. 4) decays much faster with increasing current levels than for {Mn$_4$}. Therefore, only three different current levels with a spacing of $\Delta\varepsilon \sim 50\,\mu eV$ are identified.

The larger spin polarization and orbital momentum in the {Co$_4$}-CNT, predicted by DFT, will result in a response to an external magnetic field. Figure 5(a) presents a part of the stability diagram of the {Co$_4$} device taken at $B = 8\,T$. Each line is split into two compared with Fig. 2(b) and corresponds to different Zeeman levels of the CNT quantum dot with $\Delta E_{Zee} = 0.8\,meV$. No RTS is observed when $dI/dV = 0$, as the quantum dot serves as detector only for $dI/dV \neq 0$. Exemplary current traces measured at two positions [white dots in Fig. 5(a)] are shown in Fig. 5(b). The background noise in the Coulomb blockade and on the plateaus of the Coulomb staircase shows a Gaussian distribution, as expected [Fig. 5(b), lower trace]. Between two plateaus where the slope of the current change is steepest, the current traces exhibit a clear RTS [Fig. 5(b), upper trace].

Indeed, three different current levels with larger energy splitting than at $B = 0\,T$ are clearly identified in the respective PDF. We find that the steps between two adjacent energy
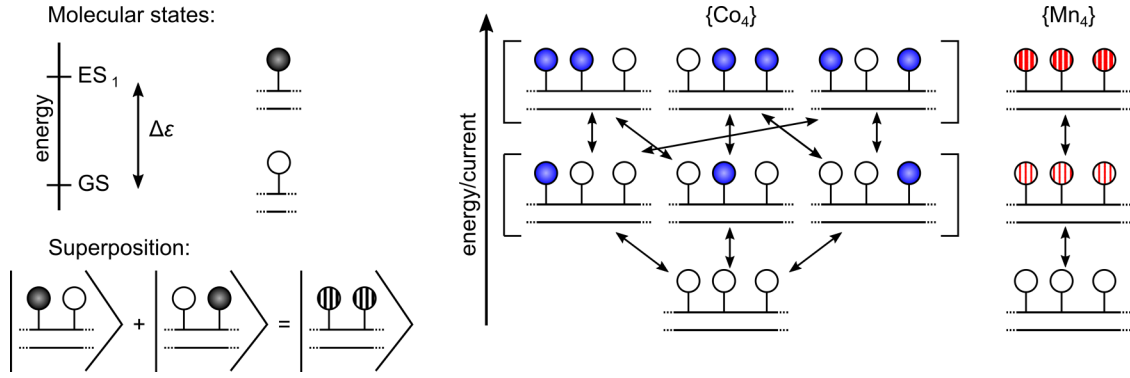
FIG. 6. Sketch of the different states of the system. Molecules can be in their ground state (open circles), the first excited state (full circles), or a superposition thereof (striped circles). The higher the current level, the more molecules are in an excited state. Here, only three of the attached molecules are shown with the possible transitions. In the case of {Co$_4$}, the different transitions are independent. For {Mn$_4$}, the states exist in a superposition, and thus, the transitions are coherent.

levels are equidistant with $\Delta\varepsilon \sim 100\,\mu\text{eV}$. Fitting three Gaussian peaks to the PDF, we find similar amplitudes for the signals with and without a magnetic field applied, cf. Fig. 4 (right) and Fig. 5(b).

D. Theoretical model

We interpret the telegraph signal in the following way: From time to time, an electron tunneling through the quantum dot provides the energy to excite the combined system of CNT quantum dot and all attached molecules. The excitation energy $\Delta\varepsilon$ is that of a single {M$_4$} complex (Fig. 6). The excited state is thereafter probed by many following electrons that experience a state-dependent tunneling rate, establishing a characteristic total current. Multiple molecules can be present in an excited state at any given time (with energy $\Delta\varepsilon$ each), leading to the multilevel PDF of the current. For relaxation, the {M$_4$} complexes dissipate their energy to the quantum-dot electrons.

The energy difference between the excited states sampled by the current in {Mn$_4$} (27 μeV) and in {Co$_4$} (100 μeV at $B = 8$ T) is orders of magnitude smaller than other processes known to cause RTS in CNT devices [43–45]. Note that these transitions do not involve spin flips, as those would require comparably large energies, since states with different spin configuration lie $\sim$2 orders of magnitude higher in energy (see Sec. SI-2 in the Supplemental Material [32]). Instead, different linear superpositions of spin pairs yielding $S_{\text{tot}}^z = 0$ differ in energy because of nonequivalent exchange interactions between them (Fig. 6 and Sec. SI-1 in the Supplemental Material [32]). Thus, we conclude that the excitation of the quantum dots is due to excitation of nondegenerate molecular $S_{\text{tot}} = 0$ eigenstates.

In the case of {Co$_4$}, we see a small dependence of the splitting on the magnetic field. We attribute this to the small residual spin and orbital momentum left on the complex (Tables S3 and S4 in the Supplemental Material [32]) as derived from DFT calculations. In total, a magnetic moment as small as $\sim$0.4 μ_B might be left on the complex leading to a Zeeman energy on the order of $\sim$100 μeV. This is an order of magnitude below the AFM coupling within the complex

[31]. Therefore, the states can still be treated as AFM with the magnetic field as a small perturbation.

The full time trace of the RTS contains more information than just the relative probability with which the different current levels occur. Since it monitors in time each transition between the different states, the RTS contains information about correlations of the switching events which, in turn, can be used to reveal details about the underlying system. In the present case, we can show that there is a fundamental difference in the excitation of the {Co$_4$} and {Mn$_4$} ensembles: For the {Co$_4$}-functionalized CNT, there are independent two-level fluctuators that can be excited individually, while for the {Mn$_4$}-functionalized CNT, the {Mn$_4$} complexes are collectively excited by forming a coherent superposition of excitations in all molecules.

To reach this conclusion, we analyze the RTS in terms of the full counting statistics. For this, we separate the time trace of the RTS into time intervals of length Δt and count the number of transitions from higher to lower levels (or equivalently from lower to higher levels). We thus obtain the probability distribution $P_N(\Delta t)$ that N transitions have occurred. This probability distribution can be characterized by so-called factorial cumulants, which are derived in the following way. First, one constructs the generating function $M_{\text{F}}(z, \Delta t) = \sum_{N=0}^{\infty} (z + 1)^N P_N(\Delta t)$, given by the z transform of the probability distribution [46–49]. Performing the mth derivative of the generating function with respect to z leads to the factorial moment of order m, which is nothing but the expectation value $\langle N(N-1)\dots(N-m+1)\rangle = \partial_z^m M_{\text{F}}(z, \Delta t)|_{z=0}$. The factorial cumulant of order m is obtained by the corresponding derivative of the logarithm of the generating function:

$$C_{\text{F},m}(\Delta t) = \langle\!\langle N(N-1)\dots(N-m+1)\rangle\!\rangle$$
$$= \partial_z^m \ln M_{\text{F}}(z, \Delta t)|_{z=0}.$$

Factorial cumulants are particularly suited to highlight deviations from a Poisson process since, for the latter, all factorial cumulants of order $m \geqslant 2$ vanish. This property also makes them resilient to detector imperfections such as limited time resolution and noise in the measurement apparatus, which may lead to missing or false counts [50].
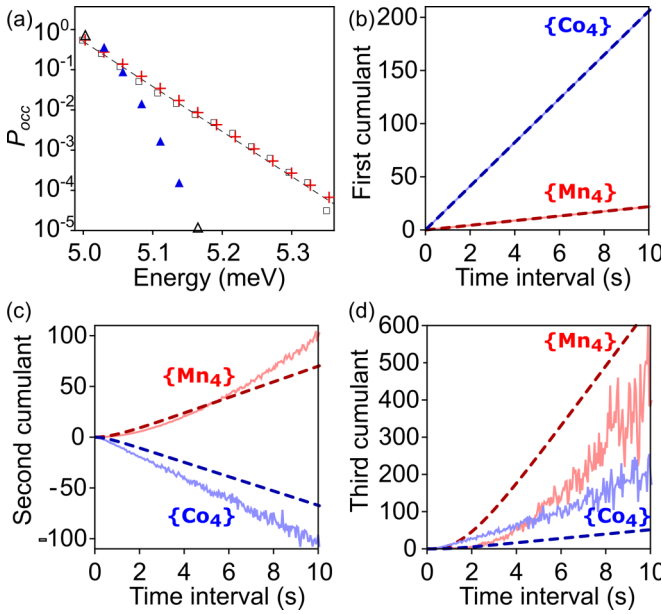
FIG. 7. (a) Occupation probability of the different levels found in the {Mn$_4$}-device on a logarithmic scale for the direct current data (black squares) and for models assuming 50 independent two-level fluctuators (blue triangles) and 50 coherently coupled two-level fluctuators (red crosses). The dashed line is a fit of the data to an exponential distribution. (b) First factorial cumulant ($C_{F,1}$) as extracted from the measurements on the carbon nanotube (CNT) quantum dots functionalized with {Mn$_4$} (red) and {Co$_4$} (blue) complexes. Fits (dashed lines) yield the transition rates used for modeling, in (c), the second ($C_{F,2}$) and, in (d), the third ($C_{F,3}$) factorial cumulant. The solid lines in (b)–(d) are the respective cumulants extracted directly from the digitized measurement signal of the two devices ({Mn$_4$}: red, {Co$_4$}: blue). The positive second cumulant in (c) is related to a super-Poissonian Fano factor by $F = (C_{F,2}/C_{F,1}) + 1$. All lines of the {Co$_4$} sample are multiplied by a factor of 20 for better visibility.

One very important feature of the factorial cumulants is that, for independent two-level fluctuators, their sign does not change as a function of time and should alternate [46–49] $C_{F,m}(\Delta t) \sim (-1)^{m-1}$, with the order m. For independent two-level fluctuators, the second factorial cumulant must be negative.

This is the case for the {Co$_4$}-functionalized CNT, see blue curves in Figs. 7(b)–7(d). Assuming 70 {Co$_4$} complexes, we extract from the first factorial cumulant the transition rates. These are used to calculate the second and third factorial cumulants [dashed lines in Figs. 7(c) and 7(d)], resulting in good agreement with the measured data at $B = 8$ T. For the {Mn$_4$}-functionalized CNT [red curves in Figs. 7(b)–7(d)], the assumption of independent two-level fluctuators can be ruled out due to the wrong sign of the second cumulant. Instead, we assume 50 {Mn$_4$} complexes that are collectively excited by forming a coherent superposition of excitations in all molecules. This model (with transition rates determined from fitting the first cumulant) correctly reproduces the second and third cumulants [Figs. 7(c) and 7(d)] as well as the exponential occupation probability distribution of the data [Figs. 7(a) and S7(b) in the Supplemental Material [32]]. The occupa-

tion probabilities P_{occ} of the levels depend on the transition rates between adjacent levels (Fig. S6 in the Supplemental Material [32]). This behavior is incompatible with independent excitations of individual {Mn$_4$} complexes, as this would yield a binomial distribution of P_{occ}. Assuming a thermally activated process, we find an activation temperature of 450 mK, in good agreement with the electron temperature of 600 mK. The signal caused by the {Co$_4$} complexes at $B = 0$ T decays too quickly for a meaningful statistical analysis. However, the occupation probability seems to behave similarly as for $B = 8$ T following a binomial decay rather than an exponential decay, which implies uncorrelated events.

Since a model of independent three-level fluctuators also fails to reproduce the data (Fig. S7b in the Supplemental Material [32]), we conclude that long-lived coherent excitations involving all {Mn$_4$} complexes are present in our system. Coherence can be obtained because the single electron at the origin of the excitation is coherent in the whole CNT quantum dot and therefore couples to all molecules at the same time. The long coherence time in the order of seconds is, indeed, likely if both the ground and excited states of the {Mn$_4$} complexes do not carry a magnetic moment that could couple to any dipolar (magnetic or electric) field.

In the {Co$_4$} device, on the other hand, the Co^{II} ions in their octahedral ligand fields possess a considerable orbital moment. Though the applied magnetic field is not large enough to change the AFM nature of the ground state (Sec. SI-2 in the Supplemental Material [32]), the residual orbital moment couples to fluctuations of dipolar fields, leading to fast decoherence due to spin-orbit coupling [51,52].

III. CONCLUSIONS

In this paper, we study the RTS of CNT quantum dots functionalized with small ensembles of two molecular analogs of AFMs, {Mn$_4$} and {Co$_4$}. While the energy changes corresponding to the transitions between different current levels are very similar for both complexes, the statistical behavior of the RTS differs fundamentally between the manganese and cobalt derivatives. As the only fundamental difference between the two complexes concerns the orbital magnetic moment, which is fully quenched in {Mn$_4$} but present in {Co$_4$}, the RTS is necessarily linked to magnetic transitions, specifically transitions between nondegenerate $S_{tot} = 0$ states of individual molecular AFMs. Based on the RTS statistics, we can show that, while complexes based on magnetic Co^{II} ions switch independently, their congeners based on Mn^{II} ions exhibit a long-lived coherent superposition between the states of all molecules attached to the quantum dot. This leads to a fundamental perspective on information processing with magnetic molecules. Molecular AFM coupling between individual molecules on the order of 100 K is well known [53]. Hence, it appears feasible to design AFM molecules with nondegenerate $S_{tot} = 0$ eigenstates that exhibit similar strong coupling, causing a larger separation in energy than the molecules presented here, enough to prevent switching between states caused by temperature. Instead, by inducing dipolar moments, Raman transitions could be driven to change states deliberately. Alternatively, similar control could be

reached using tunable exchange interactions J_{ij} to modify the energetic order of $S_{tot} = 0$ states. The difference in behavior of both molecular systems investigated here reveals the large impact of even small residual orbital moments on the spin coherence in molecular AFMs. In the complete absence of such moments, strikingly long coherence times on the order of seconds can be achieved. The coupling of the molecules to each other is mediated exclusively by the small but long-ranged spin polarization transferred to the conduction electrons of the CNT. This offers means of controlling the device: Using ferromagnetic contacts, spin-polarized electrons can be injected into the CNT [54], and the spin polarization of the conduction electrons can be controlled using a gate [55].

APPENDIX A: ATOMISTIC SIMULATIONS

First-principles simulations of the $\{M_4\}$-CNT systems (with M = Mn, Co) were performed using the SIESTA [56] implementation of DFT, within the local spin-density approx-

imation. The $\{M_4\}$ complexes are bound via a carboxylate $(-CO_2^-)$ group to the dangling C of a monovacancy site on the external wall of a metallic armchair (5,5) nanotube. The choice of a metallic nanotube ensures that electron conduction is allowed around the Fermi energy. We have shown that the oxygenated vacancy is especially favorable for functionalization of CNTs with CO_2 [7] or magnetic nanoparticles [8]. We performed simulations of a single molecule grafted to an infinite tube using the open-system setup of Ref. [9], combining the nonequilibrium Green's function formalism with a DFT Hamiltonian as implemented in TRANSIESTA [57]. This is necessary to avoid artifacts resulting from the long-range character of the indirect exchange coupling between magnetic clusters mediated by the conduction electrons of the CNT [58]. The simulation setup was composed of a central region of 35 CNT rings (86 Å long) contacted by two semi-infinite (5,5)-CNTs on each side. The spin-orbit coupling was introduced using the formalism of Ref. [36], as implemented in SIESTA [59]. Further technical details are provided in Sec. SI-2 in the Supplemental Material [32].

APPENDIX B: DEVICE FABRICATION

Electronic devices were fabricated as described in Ref. [39]. Briefly, isolated single-wall CNTs were grown on a Si/SiO_2 substrate using methane as a feedstock and Fe/Mo catalyst nanoparticles. The nanotubes were oxidized in air at $450°C$, and then the field-effect-transistor structure of the quantum-dot device was fabricated using the substrate as a back gate and Pt leads ($\{Mn_4\}$-based devices), or the device was fabricated and then the nanotubes oxidized ($\{Co_4\}$-based devices). Here, $[M_4L_2(OAc)_4]$ complexes ($H_2L = 2,6$-bis-[1-(2-hydroxyphenyl)iminoethyl]pyridine, $\{Mn_4\}$ and $\{Co_4\}$) were synthesized according to the literature [29,30] and bonded to the nanotubes by introducing the device into a solution of the complex (in acetonitrile solution for $\{Mn_4\}$, in dichloromethane for $\{Co_4\}$) for a week before rinsing away the noncovalently attached complexes over another week. A density of functionalization of ~ 1 molecule/10 nm was achieved [31].

APPENDIX C: ELECTRONIC MEASUREMENTS

All electronic measurements were carried out in a $^3He/^4He$ dilution refrigerator at a base temperature ~ 100 mK. The bias voltage was supplied symmetrically via digital-to-analog converters, addressed via an optical fiber to decouple it from the mains. The electron temperature was determined from the width of the Coulomb peaks and independently by fitting a Fermi function to the first current step (ground-state tunneling) of the Coulomb staircase taken from the $\{Co_4\}$-CNT stability diagram. The current of the noise traces was amplified using a low-noise current-to-voltage (IV) converter (QT-IVVI Rack, TU-Delft) and was measured by averaging over 20 ms (NPLC 1) using an HP34401A multimeter. In total, we had four devices (one based on $\{Mn_4\}$, three based on $\{Co_4\}$) that exhibited regular Coulomb diamonds after cooldown. All of them exhibited RTSs. Two of the devices are discussed in this paper.

APPENDIX D: RAMAN SPECTROSCOPY

Confocal micro-Raman spectroscopy was performed at room temperature in backscattering geometry with a Horiba Jobin Yvon LabRAM HR800 monochromator. For this, a He-Ne laser emitting at 633 nm was focused through a 100× microscope objective with 0.95 NA, and the power was kept at 0.7 mW (as measured before the objective). With the help of previously acquired scanning electron microscope images of the device [39], the sample was oriented such that the nanotube is aligned parallel to the laser polarization to maximize the signal. The target area was mapped with a motorized stage to find the precise position of the nanotube through its Raman signal, and the depth focus was subsequently adjusted on the nanotube for maximal intensity.

The Raman spectra were spectrally calibrated by the emission lines of a neon lamp. The background signal that is caused by Raman scattering with the silicon wafer of the device was measured with $\sim 2\,\mu$m lateral distance to the nanotube, which allowed for subsequent subtraction from the signal.

APPENDIX E: DATA ANALYSIS

We used the histogram of the derivative of the direct current data (before background correction) of the {Mn$_4$}-functionalized device to determine current steps of $\Delta I \approx 80$ pA with a standard deviation of $\sigma_{\text{direct}} = 40(1)$ pA [see Fig. 3(b)]. To digitize the RTS, the background of the noise traces was removed using the statistics-sensitive nonlinear iterative peak clipping algorithm implemented in the computer algebra system Wolfram Mathematica. The PDFs and cumulants were determined from a current time trace of 1300 s (3600 s) length for the {Co$_4$}-functionalized ({Mn$_4$}-functionalized) device. The models used to simulate the data are elaborated in the Supplemental Material [32].

[1] Upping the anti, Nat. Phys. **14**, 199 (2018).

[2] V. Baltz, A. Manchon, M. Tsoi, T. Moriyama, T. Ono, and Y. Tserkovnyak, Antiferromagnetic spintronics, Rev. Mod. Phys. **90**, 015005 (2018).

[3] T. Jungwirth, X. Marti, P. Wadley, and J. Wunderlich, Antiferromagnetic spintronics, Nat. Nanotechnol. **11**, 231 (2016).

[4] C. Marrows, Addressing an antiferromagnetic memory, Science **351**, 558 (2016).

[5] M. Atzori and R. Sessoli, The second quantum revolution: Role and challenges of molecular chemistry, J. Am. Chem. Soc. **141**, 11339 (2019).

[6] M. Gobbi, M. A. Novak, and E. del Barco, Molecular spintronics, J. Appl. Phys. **125**, 240401 (2019).

[7] Z. Zanolli and J. C. Charlier, Defective carbon nanotubes for single-molecule sensing, Phys. Rev. B **80**, 155447 (2009).

[8] Z. Zanolli and J. C. Charlier, Single-molecule sensing using carbon nanotubes decorated with magnetic clusters, ACS Nano **6**, 10786 (2012).

[9] Z. Zanolli and J. C. Charlier, Spin transport in carbon nanotubes with magnetic vacancy-defects, Phys. Rev. B **81**, 165406 (2010).

[10] S. Schmaus, A. Bagrets, Y. Nahas, T. K. Yamada, A. Bork, M. Bowen, E. Beaurepaire, F. Evers, and W. Wulfhekel, Giant Magnetoresistance through a single molecule, Nat. Nanotechnol. **6**, 185 (2011).

[11] M. Bazarnik, B. Bugenhagen, M. Elsebach, E. Sierda, A. Frank, M. H. Prosenc, and R. Wiesendanger, Toward tailored all-spin molecular devices, Nano Lett. **16**, 577 (2016).

[12] S. Karan, C. García, M. Karolak, D. Jacob, N. Lorente, and R. Berndt, Spin control induced by molecular charging in a transport junction, Nano Lett. **18**, 88 (2018).

[13] A. Bellec, J. Lagoute, and V. Repain, Molecular electronics: Scanning tunneling microscopy and single-molecule devices, C. R. Chim. **21**, 1287 (2018).

[14] F. Paschke, P. Erler, V. Enenkel, L. Gragnaniello, and M. Fonin, Bulk-like magnetic signature of individual Fe$_4$ molecular magnets on graphene, ACS Nano **13**, 780 (2019).

[15] J. Li, N. Friedrich, N. Merino, D. G. de Oteyza, D. Peña, D. Jacob, and J. I. Pascual, Electrically addressing the spin of a magnetic porphyrin through covalently connected graphene electrodes, Nano Lett. **19**, 3288 (2019).

[16] G. Czap, P. J. Wagner, F. Xue, L. Gu, J. Li, J. Yao, R. Wu, and W. Ho, Probing and imaging spin interactions with a magnetic single-molecule sensor, Science **364**, 670 (2019).

[17] G. Czap, P. J. Wagner, J. Li, F. Xue, J. Yao, R. Wu, and W. Ho, Detection of Spin-Vibration States in Single Magnetic Molecules, Phys. Rev. Lett. **123**, 106803 (2019).

[18] E. Sierda, M. Elsebach, R. Wiesendanger, and M. Bazarnik, Probing weakly hybridized magnetic molecules by single-atom magnetometry, Nano Lett. **19**, 9013 (2019).

[19] K. Yang, H. Chen, T. Pope, Y. Hu, L. Liu, D. Wang, L. Tao, W. Xiao, X. Fei, Y.-Y. Zhang *et al.*, Tunable giant magnetoresistance in a single-molecule junction, Nat. Commun. **10**, 3599 (2019).

[20] Z. Xu, J. Liu, S. Hou, and Y. Wang, Manipulation of molecular spin state on surfaces studied by scanning tunneling microscopy, Nanomat. **10**, 2393 (2020).

[21] J. E. Grose, E. S. Tam, C. Timm, M. Scheloske, B. Ulgut, J. J. Parks, H. D. Abruña, W. Harneit, and D. C. Ralph, Tunnelling spectra of individual magnetic endofullerene molecules, Nat. Mater. **7**, 884 (2008).

[22] R. Vincent, S. Klyatskaya, M. Ruben, W. Wernsdorfer, and F. Balestro, Electronic read-out of a single nuclear spin using a molecular spin transistor, Nature **488**, 357 (2012).

[23] S. Thiele, F. Balestro, R. Ballou, S. Klyatskaya, M. Ruben, and W. Wernsdorfer, Electrically driven nuclear spin resonance in single-molecule magnets, Science **344**, 1135 (2014).

[24] E. Burzurí, A. García-Fuente, V. García-Suárez, K. Senthil Kumar, M. Ruben, J. Ferrer, and H. S. J. van der Zant, Spin-state dependent conductance switching in single molecule-graphene junctions, Nanoscale **10**, 7905 (2018).

[25] L. Bogani and W. Wernsdorfer, Molecular spintronics using single-molecule magnets, Nat. Mater. **7**, 179 (2008).

[26] M. Urdampilleta, S. Klyatskaya, J. P. Cleuziou, M. Ruben, and W. Wernsdorfer, Supramolecular spin valves, Nat. Mater. **10**, 502 (2011).

[27] M. Ganzhorn, S. Klyatskaya, M. Ruben, and W. Wernsdorfer, Strong spin-phonon coupling between a single-molecule magnet and a carbon nanotube nanoelectromechanical system, Nat. Nanotechnol. **8**, 165 (2013).

[28] M. Urdampilleta, S. Klyatskaya, M. Ruben, and W. Wernsdorfer, Magnetic interaction between a radical spin and a single-molecule magnet in a molecular spin-valve, ACS Nano **9**, 4458 (2015).

[29] E. Kampert, F. F. B. J. Janssen, D. W. Boukhvalov, J. C. Russcher, J. M. M. Smits, R. de Gelder, B. de Bruin, P. C. M. Christianen, U. Zeitler, M. I. Katsnelson *et al.*, Ligand-controlled magnetic interactions in Mn_4 clusters, lnorg. Chem. **48**, 11903 (2009).

[30] S. Achilli, C. Besson, X. He, P. Ordejón, C. Meyer, and Z. Zanolli, Magnetic properties of coordination clusters with {Mn_4} and {Co_4} antiferromagnetic cores, Phys. Chem. Chem. Phys. **24**, 3780 (2022).

[31] R. Frielinghaus, C. Besson, L. Houben, A.-K. Saelhoff, C. M. Schneider, and C. Meyer, Controlled covalent binding of antiferromagnetic tetramanganese complexes to carbon nanotubes, RSC Adv. **5**, 84119 (2015).

[32] See Supplemental Material at http://link.aps.org/supplemental/10.1103/PhysRevB.107.245414 for a discussion of spin states in the {M_4} complex, DFT calculations of {Mn_4} or {Co_4} complex grafted to the CNT, a Raman spectrum of the {Mn_4} functionalized CNT device, the histogram of the derivative of the original direct current data, the theoretical models and results (PDF file) as well as the coordinates of CNT-{M_4} systems used for DFT calculations (ZIP archive containing separate XYZ files). The Supplemental Material also contains additional Refs. [33–38].

[33] N. L. Johnson, A. W. Kemp, and S. Kotz, *Univariate Discrete Distributions* (John Wiley & Sons, Inc., Hoboken, 2005).

[34] S. Reich, C. Thomsen, and J. Maultzsch, *Carbon Nanotubes: Basic Concepts and Physical Properties* (Wiley-VCH Verlag GmbH & Co. KGaA, Weinheim, 2004).

[35] M. Brandbyge, J.-L. Mozos, P. Ordejón, J. Taylor, and K. Stokbro, Density-functional method for nonequilibrium electron transport, Phys. Rev. B **65**, 165401 (2002).

[36] R. Cuadrado and J. I. Cerdá, Fully relativistic pseudopotential formalism under an atomic orbital basis: Spin-orbit splittings and magnetic anisotropies, J. Phys.: Condens. Matter **24**, 086005 (2012).

[37] S. L. Dudarev, G. A. Botton, S. Y. Savrasov, C. J. Humphreys, and A. P. Sutton, Electron-energy-loss spectra and the structural stability of nickel oxide: An LSDA+U study, Phys. Rev. B **57**, 1505 (1998).

[38] J. M. Soler, E. Artacho, J. D. Gale, A. García, J. Junquera, P. Ordejón, and D. Sanchez-Portal, The SIESTA method for *ab initio* order-N materials simulation, J. Phys.: Condens. Matter **14**, 2745 (2002).

[39] M. Schnee, C. Besson, R. Frielinghaus, C. Lurz, P. Kögerler, C. M. Schneider, and C. Meyer, Quantum transport in carbon nanotubes covalently functionalized with magnetic molecules, Phys. Status Solidi B **253**, 2424 (2016).

[40] S. Piscanec, M. Lazzeri, J. Robertson, A. C. Ferrari, and F. Mauri, Optical phonons in carbon nanotubes: Kohn anomalies, Peierls distortions, and dynamic effects, Phys. Rev. B **75**, 035427 (2007).

[41] A. Vierck, F. Gannott, M. Schweiger, J. Zaumseil, and J. Maultzsch, ZA-derived phonons in the Raman spectra of single-walled carbon nanotubes, Carbon **117**, 360 (2017).

[42] M. Bockrath, D. H. Cobden, P. L. McEuen, N. G. Chopra, A. Zettl, A. Thess, and R. E. Smalley, Single-electron transport in ropes of carbon nanotubes, Science **275**, 1922 (1997).

[43] V. A. Sydoruk, K. Goß, C. Meyer, M. V. Petrychuk, B. A. Danilchenko, P. Weber, C. Stampfer, J. Li, and S. A. Vitusevich, Low-frequency noise in individual carbon nanotube field-effect transistors with top, side and back gate configurations: Effect of gamma irradiation, Nanotechnology **25**, 035703 (2013).

[44] S. Ponzoni, S. Achilli, C. Pintossi, G. Drera, L. Sangaletti, P. Castrucci, M. De Crescenzi, and S. Pagliara, Hybridized C–O–Si interface states at the origin of efficiency improvement in CNT/Si solar cells, ACS Appl. Mater. Interfaces **9**, 16627 (2017).

[45] A. Gruneis, M. J. Esplandiu, D. Garcia-Sanchez, and A. Bachtold, Detecting individual electrons using a carbon nanotube field-effect transistor, Nano Lett. **7**, 3766 (2007).

[46] D. Kambly, C. Flindt, and M. Büttiker, Factorial cumulants reveal interactions in counting statistics, Phys. Rev. B **83**, 075432 (2011).

[47] P. Stegmann, B. Sothmann, A. Hucht, and J. König, Detection of interactions via generalized factorial cumulants in systems in and out of equilibrium, Phys. Rev. B **92**, 155413 (2015).

[48] A. Kurzmann, P. Stegmann, J. Kerski, R. Schott, A. Ludwig, A. D. Wieck, J. König, A. Lorke, and M. Geller, Optical Detection of Single-Electron Tunneling into a Semiconductor Quantum Dot, Phys. Rev. Lett. **122**, 247403 (2019).

[49] P. Stegmann and J. König, Short-time counting statistics of charge transfer in Coulomb-blockade systems, Phys. Rev. B **94**, 125433 (2016).

[50] E. Kleinherbers, P. Stegmann, A. Kurzmann, M. Geller, A. Lorke, and J. König, Pushing the Limits in Real-Time Measurements of Quantum Dynamics, Phys. Rev. Lett. **128**, 087701 (2022).

[51] A. V. Khaetskii and Y. V. Nazarov, Spin relaxation in semiconductor quantum dots, Phys. Rev. B **61**, 12639 (2000).

[52] M. Martens, G. Franco, N. S. Dalal, S. Bertaina, and I. Chiorescu, Spin-orbit coupling fluctuations as a mechanism of spin decoherence, Phys. Rev. B **96**, 180408(R) (2017).

[53] M. Serri, W. Wu, L. R. Fleet, N. M. Harrison, C. F. Hirjibehedin, C. W. M. Kay, A. J. Fisher, G. Aeppli, and S. Heutz, High-temperature antiferromagnetism in molecular semiconductor thin films and nanostructures, Nat. Commun. **5**, 3079 (2014).

[54] C. Morgan, M. Misiorny, D. Metten, S. Heedt, T. Schäpers, C. M. Schneider, and C. Meyer, Impact of Tunnel-Barrier Strength on Magnetoresistance in Carbon Nanotubes, Phys. Rev. Appl. **5**, 054010 (2016).

[55] M. Misiorny and C. Meyer, Gate-Voltage Response of a One-Dimensional Ballistic Spin Valve without Spin-Orbit Interaction, Phys. Rev. Appl. **7**, 024011 (2017).

[56] A. García, N. Papior, A. Akhtar, E. Artacho, V. Blum, E. Bosoni, P. Brandimarte, M. Brandbyge, J. I. Cerdá, F. Corsetti

et al., SIESTA: Recent developments and applications, J. Chem. Phys. **152**, 204108 (2020).

[57] N. Papior, N. Lorente, T. Frederiksen, A. García, and M. Brandbyge, Improvements on non-equilibrium and transport Green function techniques: The next-generation TRANSIESTA, Comput. Phys. Commun. **212**, 8 (2017).

[58] A. T. Costa, D. F. Kirwan, and M. S. Ferreira, Indirect exchange coupling between magnetic adatoms in carbon nanotubes, Phys. Rev. B **72**, 085402 (2005).

[59] R. Cuadrado, R. Robles, A. García, M. Pruneda, P. Ordejón, J. Ferrer, and J. I. Cerdá, Validity of the on-site spin-orbit coupling approximation, Phys. Rev. B **104**, 195104 (2021).